Influenza Virus Infection Model With Density Dependence Supports Biphasic Viral Decay

Amanda P. Smith[1], David J. Moquin[2], Veronika Bernhauerova[3], and Amber M. Smith[1,*]

[1]*Department of Pediatrics, University of Tennessee Health Science Center, Memphis, TN 38163, USA*
[2]*Department of Internal Medicine, University of Tennessee Health Science Center, Memphis, TN 38163, USA*
[3]*Institut Pasteur, Viral Populations and Pathogenesis Unit, Paris, FR*
[*]*amber.smith@uthsc.edu*

Abstract

Mathematical models that describe infection kinetics help elucidate the time scales, effectiveness, and mechanisms underlying viral growth and infection resolution. For influenza A virus (IAV) infections, the standard viral kinetic model has been used to investigate the effect of different IAV proteins, immune mechanisms, antiviral actions, and bacterial coinfection, among others. We sought to further define the kinetics of IAV infections by infecting mice with influenza A/PR8 and measuring viral loads with high frequency and precision over the course of infection. The data highlighted dynamics that were not previously noted, including viral titers that remain elevated for several days during mid-infection and a sharp 4–5 $\log_{10}$ decline in virus within one day as the infection resolves. The standard viral kinetic model, which has been widely used within the field, could not capture these dynamics. Thus, we developed a new model that could simultaneously quantify the different phases of viral growth and decay with high accuracy. The model suggests that the slow and fast phases of virus decay are due to the clearance rate changing as the density of infected cells changes. To characterize this model, we fit the model to the viral load data, examined the parameter behavior, and connected the results and parameters to linear regression estimates. The resulting parameters and model dynamics revealed that the rate of viral clearance during resolution occurs 25 times faster than the clearance during mid-infection and that small decreases to this rate can significantly prolong the infection. This likely reflects the high efficiency of the adaptive immune response. The new model provides a well-characterized representation of IAV infection dynamics, is useful for analyzing and interpreting viral load dynamics in the absence of immunological data, and further insight into the regulation of viral control.

Introduction

Influenza A virus (IAV) is a leading cause of lower respiratory tract infections and causes a significant amount of morbidity and mortality [18, 25, 34], with over 15 million individuals infected and more than 200,000 hospitalizations each year in the U.S. [35]. Vaccination against influenza viruses remains the most effective measure to prevent infection, but the large number of antigenically distinct strains, the emergence of new strains, and the low efficacy of antivirals make combatting the disease challenging. New therapeutic strategies are thus necessary and may require modulation of different viral control mechanisms, which are not entirely understood for IAV infection. Thus, it is critical to gain a deeper understanding of the infection kinetics, including determining

1

the time scales, magnitudes, contribution, and interrelatedness of different control processes throughout IAV infection.

Kinetic modeling of *in vivo* infection processes provides important insight into viral growth and decay, host immune responses, antiviral actions, and multi-pathogen interactions. Remarkably, as few as 3-4 equations for target cells, infected cells, and virus can accurately describe viral load dynamics for a variety of virus infections (e.g., IAV, HIV, HCV, Zika virus, and West Nile Virus [1, 2, 5, 20, 22]). For IAV infections, numerous studies have used these simple models with great success to elucidate mechanisms during IAV infection and during IAV coinfection with bacterial pathogens (reviewed in [3, 7, 27–29]). However, investigating mechanisms of immune control is often inhibited by insufficient data, which limits effective model calibration and selection. Further, it can be difficult to distinguish between mechanisms because a viral kinetic model that excludes equations and terms for specific immune responses can fit viral load dynamics with ease.

To aid interpretation of model results and gain insight into the mechanisms of infection, previous studies have used linear regression and approximate solutions to the viral kinetic model to identify how different processes (e.g., virus infection, production, and clearance) contribute to viral load dynamics throughout the course of infection. In the initial hours of infection, virus quickly infects cells or is cleared. Following an eclipse phase, virus production begins and virus increases exponentially for ~2–3 d. This initial growth can be approximated by a linear function of the $\log_{10}$ viral titers or by $V(t) = e^{\lambda t}$, where λ is a combination of all infection processes and is equivalent to the log-linear slope [31, 32]. After this growth phase, virus peaks and begins to decline until the infection is resolved. Virus decay is typically exponential in nature and can be approximated in a similar fashion as the growth phase. That is, $V(t) = e^{-\delta t}$, where δ is the infected cell death rate and the sole process dictating the viral decay dynamics. Here, the log-linear slope is an estimate of the infected cell death rate [31, 32].

Although these dynamics and approximations have improved our knowledge of viral kinetics, some dynamical features, such as the plateauing of virus following the peak (reviewed in [28]) cannot be explained by current kinetic models that exclude equations for immune factors. One model could reproduce the plateauing of virus through modeling interferon and an interferon-induced adaptive immune response [21]. The study concluded that specific equations for the innate and adaptive responses were necessary. However, quantitative immunological data was not used to support model selection, parameterization, and conclusions. This type of data is scarce and has been a limiting factor of modeling studies. With viral loads as the most prevalent type of data, models that limit the number of parameters and equations remain desirable.

To gain deeper insight into the mechanisms of viral resolution and improve predictive power of kinetic models, we measured viral loads daily from the lungs of BALB/cJ mice infected with influenza A/Puerto Rico/8/34 (H1N1) (PR8). In addition, we tightly controlled the experimental conditions and repeated the experiment

2

numerous times to ensure reproducibility and identify data with true biological heterogeneity versus data with experimental heterogeneity. The high resolution of these data defined important dynamical features, including a long plateau phase followed by a rapid decay phase. Because current viral kinetic models could not reproduce these data, we developed a new model that incorporated a density-dependent decay of infected cells and could accurately describe the observed viral load dynamics. We used a rigorous fitting scheme to estimate the model parameters and infer important dynamics. Subsequent linear regression analysis and sensitivity analysis aided effective interpretation of the model results and direct comparison with published results. The data, model, and analyses provide a robust quantification of IAV infection kinetics and indicate that the rate of virus clearance changes with respect to the density of infected cells.

Materials and Methods

Use of Experimental Animals

All experimental procedures were approved by the Animal Care and Use Committee at SJCRH under relevant institutional and American Veterinary Medical Association guidelines and were performed in a Biosafety level 2 facility that is accredited by AALAAS.

Mice

Adult (6 week old) female BALB/cJ mice were obtained from Jackson Laboratories (Bar Harbor, ME). Mice were housed in groups of 5 mice in high-temperature 31.2cm $\times$ 23.5cm $\times$ 15.2cm polycarbonate cages with isolator lids. Rooms used for housing mice were maintained on a 12:12-hour light:dark cycle at $22 \pm 2°$C with 50% humidity in the biosafety level 2 facility at St. Jude Children's Research Hospital (Memphis, TN). Prior to inclusion in the experiments, mice were allowed at least 7 days to acclimate to the animal facility such that they were 7 weeks old at the time of infection. Laboratory Autoclavable Rodent Diet (PMI Nutrition International, St. Louis, MO) and autoclaved water were available ad libitum. All experiments were performed under an approved protocol and in accordance with the guidelines set forth by the Animal Care and Use Committee at St. Jude Children's Research Hospital.

Infectious Agents

All experiments were done using the mouse adapted influenza A/Puerto Rico/8/34 (H1N1) (PR8).

Infection Experiments

The viral infectious dose ($TCID_{50}$) was determined by interpolation using the method of Reed and Muench [23] using serial dilutions of virus on Madin-Darby canine kidney (MDCK) cells. Mice were intranasally inoculated with 75 $TCID_{50}$ PR8 in 100 µl. Mice were weighed at the onset of infection and each subsequent day for illness and mortality. Mice were euthanized if they became moribund or lost 30% of their starting body weight. We repeated each experiment at least one time to ensure reproducibility.

Lung Titers

Mice were euthanized by CO_2 asphyxiation. Lungs were aseptically harvested, washed three times in PBS, and placed in 500 µl sterile PBS. Whole lungs were digested with collagenase (1mg/ml, Sigma C0130), and physically homogenized by syringe plunger against a 40 µm cell strainer. Cell suspensions were centrifuged at 4°C, 500 × g for 7 min. The supernatants were used to determine the viral titers using serial dilutions on MDCK monolayers.

Mathematical Model

The standard viral kinetic model used to describe IAV infection kinetics tracks 4 populations: susceptible epithelial ("target") cells (T), two classes of infected cells (I_1 and I_2), and virus (V) [1]:

$$\frac{dT}{dt} = -\beta TV \tag{1}$$

$$\frac{dI_1}{dt} = \beta TV - kI_1 \tag{2}$$

$$\frac{dI_2}{dt} = kI_1 - \delta(I_2)I_2 \tag{3}$$

$$\frac{dV}{dt} = pI_2 - cV \tag{4}$$

In this model, target cells become infected with virus at rate βV per cell. Once infected, these cells enter an eclipse phase (I_1) at rate k per cell before transitioning to produce virus at rate p per cell (I_2). Virus is cleared at rate c and virus-producing infected cells (I_2) are cleared according to the function $\delta(I_2)$. The original model assumes that infected cells are cleared at a constant rate ($\delta(I_2) = \delta_s$) [1]. Here, we modify this model and let the clearance rate vary with the number of infected cells such that

$$\delta(I_2) = \frac{\delta_d}{K_\delta + I_2}, \tag{5}$$

where δ_d/K_δ is the maximum rate of infected cell clearance and K_δ is the half-saturation constant.

4

Parameter Estimation

Given a parameter set θ, the cost $C(\theta) = \sum_{v_i}(V(\theta, t_i) - v_i)^2$ was minimized across parameter ranges using an Adaptive Simulated Annealing (ASA) global optimization algorithm (details in the Supplementary Material) to compare experimental and predicted values of $\log_{10} \text{TCID}_{50}/\text{lung}$. Errors of the $\log_{10}$ data were assumed to be normally distributed. To explore and visualize the regions of parameters consistent with the models, we fit Equations (1)–(5) to 1000 bootstrap replicates of each data set. For each bootstrap data set, the model was fit 10 times beginning from the best-fit parameters estimate θ^{best} that was found by fitting the model to the data then perturbing each parameter estimate uniformly within $\pm 50\%$. If the three best bootstrap fits were within 0.05 of the best-fit, then the bootstrap was considered successful. For each best fit estimate, we provide 95% confidence interval (CI) computed from the bootstrap replicates. All calculations were performed in MATLAB.

Bounds were placed on the parameters to constrain them to physically realistic values. Because biological estimates are not available for all parameters, ranges were set reasonably large based on preliminary results and previous estimates [32]. The rate of infection (β) was allowed to vary between 10^{-6} TCID_{50}^{-1} d^{-1} and 10^{-1} TCID_{50}^{-1} d^{-1}, and the rate of viral production (p) between 10^{-1} TCID_{50} cell^{-1} d^{-1} and 10^3 TCID_{50} cell^{-1} d^{-1}. Bounds for the viral clearance rate (c) were 1 d^{-1} ($t_{1/2} = 16.7$ h) and 10^3 d^{-1} ($t_{1/2} = 1$ min). Previous estimates of the eclipse phase rate (k) for IAV infection in mice resulted in estimates that fell outside the biologically feasible range of 4-6 h [32]. To insure biological feasibility, the lower and upper bounds for the eclipse phase rate (k) were 4 d^{-1} and 6 d^{-1}. Limits for the half-saturation constant (K_δ) were $10^2 - 10^6$ cells, and limits for the infected cell clearance parameter (δ_d) were $1 - 4 \times 10^6$ cells/d.

The initial number of target cells (T_0) was set to 10^7 cells [32, 33]. Because the initial viral inoculum rapidly infects cells and/or is cleared within 4 h pi, as indicated by the undetectable viral titers at this time point (Figure 1), the initial number of infected cells $I_1(0)$ was set to 75 cells to reflect an initial dose of 75 TCID_{50}. This is an alteration from previous studies, including our own, that either estimate the initial amount of virus (V_0) or set its value to the true viral inoculum. Fixing $V(0) = 75$ TCID_{50} or estimating its value did not improve the fit and could not be statistically justified (see, for example, Table S1). Estimating $I_1(0)$ could also not be justified and did not improve the model fit (e.g., as in Table S1 and Figure S3). The initial number of productively infected cells ($I_2(0)$) and the initial free virus (V_0) were set to 0.

Linear Regression

We used the function *polyfit* in MATLAB to perform linear regression of the $\log_{10}$ values of viral titer during the growth phase (4h, 1-2 d pi) and the two decay phases (3-6 d pi and 7-8 d pi). No data point was allowed to be included in two phases.

5

Results

Phases of Viral Load Kinetics

Mice infected with 75 $TCID_{50}$ PR8 have viral load kinetics that can be separated into five distinct phases (Figure 1). This is in contrast to the three phases that we previously defined [31]. In the first phase, virus quickly infects cells and is undetectable within 4 h pi. In the second and third phases, virus increases exponentially and peaks after $\sim$2–3 d pi. Following the peak, the viral decline can be separated into two phases. In the first decay phase (3–7 d pi), virus decays slowly at a relatively constant rate. In the second decay phase (7–8 d pi), virus declines rapidly (4–5 $\log_{10}$ $TCID_{50}$). Sixty percent of mice had no detectable virus by 8 d pi. The remaining mice resolved the infection by 9 d pi.

These data reduced the heterogeneity observed in a previous data set from infection with the same virus [32]. We discovered that the majority of heterogeneity in the previous data set could be attributed to inconsistent infections and, thus, inocula that varied. We further reduced heterogeneity by normalizing the viral titer to the total lung volume, rather than using units of $TCID_{50}$/ml lung homogenate. As expected, some heterogeneity remains at 1 d pi and at 8 d pi. These time points correspond to when virus is rapidly increasing and decreasing, respectively.

Kinetic Model with Density Dependent Viral Clearance

We first fit the standard viral kinetic model, which is given by Equations (1)–(4) and assumes only one mechanism of constant clearance ($\delta(I_2) = \delta_s$) [1], to the viral load data. This model was unable to capture the entire time course of viral load dynamics, but was able to fit the data from infection initiation to 7 d pi (Figure S3). To more accurately model IAV kinetics and simultaneously recapitulate the two phases of viral decline, we modified the rate of infected cell clearance ($\delta(I_2)$) so that the rate changes with respect to the density of the infected cell population (Figure 4A). That is, $\delta(I_2) = \delta_d/(K_\delta + I_2)$ (Equation (5)), where δ_d/K_δ is the maximum rate of clearance and K_δ is the number of infected cells where the rate is half of its maximum.

Fitting this new model to the viral load data illustrated that the model can accurately reproduce the data and simultaneously capture both phases of viral decline while excluding specific immune responses. The resulting dynamics are shown in Figure 1, the parameter values and 95% confidence intervals (CIs) are given in Table 1, and the parameter ensembles are shown in Figures 2 and S2. For this model, the basic reproduction number (R_0) is given by

$$R_0 = \frac{\beta p T_0 K_\delta}{c \delta_d} \tag{6}$$

Given the parameters in Table 1, $R_0 = 7.4$.

To understand how the addition of $\delta(I_2) = \delta_d/(K_\delta + I_2)$ influences the other parameters during the fitting scheme, we plotted the resulting histograms and 2D parameter projections (Figure 2). As expected, strong correlations exist between the rates of virus production (p) and virus clearance (c) and between the rate of infection (β) and the infected cell death rate (δ_d/K_δ). The other correlations visible in Figure 2 were a consequence of these two relations. Of note, δ_d was not strongly correlated with any of the other model parameters (Figure S2). In addition, the confidence interval was small, particularly compared to the other parameters. Estimates for the other parameters (β, p, c, and K_δ) with the exception of the eclipse phase rate (k) were well bounded such that the 95% CIs fell within the upper and lower bounds imposed in the estimation scheme. Similar to previous studies [1, 32], the eclipse phase rate (k) was not well defined. In support, the ASA algorithm search patterns show a longer search time for k compared to the other parameters (Figure S1).

To further determine how the addition of $\delta(I_2) = \delta_d/(K_\delta + I_2)$ influences the sensitivity of the model solution to changes in parameter values, we performed a one-at-a-time sensitivity analysis (Figure 3). The infected cell clearance parameter (δ_d) is the most sensitive parameter and largely dictates the viral decay. Decreasing δ_d significantly delays viral clearance while increasing δ_d leads to rapid viral resolution (Figure 3). In accordance with previous results [31], all other parameters are less sensitive and collectively affect the exponential growth phase and peak.

As illustrated in Figure 4A, the rate of infected cell clearance is rapid when these cells are in small numbers. Given the parameters in Table 1, the maximum clearance rate is $\delta(I_2) = 12.7$ d^{-1}, which corresponds to half-life $t_{1/2} = 1.3$ h. The rate begins to slow when $I_2 > 10^4$ cells and is minimal when I_2 is at its maximum (8×10^6 cells). When I_2 is maximal, $\delta(I_2) = 0.21$ d^{-1} and $t_{1/2} = 78$ h. In our previous work, we discovered that linear regression analysis could be used to accurately estimate the exponential growth rate, which was a combination of all model parameters, and that the slope of the viral decay could provide an estimate of $\delta(I_2)$ [31, 32]. To evaluate how these relations correlate to parameters in the model with density dependence, we performed a linear regression on the data during the growth phase (4 h – 2 d pi) and the two decay phases (3–6 d pi and 7–8 d pi) (Figure 4B). The slope of the growth phase is 3.2 $\log_{10}$ TCID$_{50}$/d (red line in Figure 4B). In accordance with the previous studies, this slope is a good approximation to the model until shortly before the peak. The model then begins to deviate from this estimate and suggests that the virus growth rate briefly increases prior to the peak. This nonlinearity in the growth can be attributed to the decreasing infected cell clearance rate as the number of infected cells increases. These results are in contrast to the standard viral kinetic model, which suggests that the virus growth rate decreases prior to the peak [31, 32]. In the first phase of decay, the slope is -0.2 $\log_{10}$ TCID$_{50}$/d (green line in Figure 4B), which corresponds to $\delta(I_2) = 0.4$ d^{-1} (green diamond in Figure 4A). In the second phase of decay, the slope is -3.8 $\log_{10}$ TCID$_{50}$/d (blue line in Figure 4B), which corresponds to $\delta(I_2) = 8.7$ d^{-1} (blue dot in Figure 4A).

Discussion

Mathematical models have been widely used to investigate IAV dynamics (reviewed in Refs. [3, 7, 27–29]). The viral kinetic model given by Equations (1)–(4) with $\delta(I_2) = \delta_s$ [1] has been the standard in the field for over 10 years. We previously used this model together with data from murine infection to gain insight into IAV virulence factors [32] and into coinfection with bacterial pathogens [26, 30, 33]. Although some predictions made using this model have been experimentally tested and deemed accurate [10, 27, 30, 37], the data here suggested that some dynamical features could not be accounted for and thus a new model was necessary. The model we introduced here includes density-dependent infected cell clearance and better captures the entire course of IAV infection dynamics, including the two-phase viral decay following the peak (Figures 1). Importantly, the model added only a single parameter (the half-saturation constant, K_δ) while significantly improving the model fit to viral loads from IAV infection without including additional equations detailing immune responses

By sampling with high frequency and controlling for experimental heterogeneity, we were able to obtain more accurate data (i.e., smaller standard deviations and better reproducibility) that highlighted several important dynamics, some of which were not previously observed. Our data showed that viral loads are maintained at a high level between 2 d and 7 d pi (Figure 1). Sustained viral loads have been observed in several studies [6, 9, 14, 16, 24, 32, 36]. In some data sets, the peak appears more pronounced and is often followed by the plateau phase or a second, lower peak [1, 4, 6, 9, 13, 14, 16]. Our murine data do not indicate a second peak, although there is a subtle increase in viral loads at 5 d pi. Previous modeling studies suggest that these dynamics required equations/terms for the innate and adaptive immune responses [1, 8, 21]. Importantly, our model here provides a means for capturing the changes in viral load decay without complicating the model or inferring information about specific immune mechanisms, which are not well understood. However, the change in clearance rate could reflect the change from innate to adaptive immunity. If this is the case, our estimates would suggest that the adaptive response is 25 times more effective than the innate response (-0.2 $\log_{10}$ TCID$_{50}$/d between 3–6 d pi versus -3.8 $\log_{10}$ TCID$_{50}$/d between 7–8 d pi; Figure 4B).

It is well accepted that the rapid decline in virus during the second decay phase is due to the infiltration of CD8$^+$ T cells (reviewed in [11, 15, 17]). These cells typically enter the infection site between 5–6 d pi and peak between 8–9 d pi (e.g., as in [36]). The rapid rate of viral decline between 7–8 d pi suggests that these cells are highly effective. However, the initial infiltration begins 1–2 d before a change in the rate of virus decay is visible. Thus, there is a nonlinearity to this response. This may reflect a change in effectiveness proportional to the density of infected cells or to the density of T cells. A handling-time effect, which could represent the time required for immune cells to kill each infected cell and/or the time for immune cells to become activated, may slow the per capita rate of clearance. Spatial constraints (e.g., crowding effect), where the number of immune cells within an area is limited, may also play a role. In contrast, numerous clearance mechanisms

8

(e.g., interferons, macrophages, neutrophils, natural killer (NK) cells) are thought to be important during early- and mid-infection, but their contribution to the viral load kinetics is unclear. Using a model to distinguish between these mechanisms is challenging given the close fit of simple kinetic models to viral load data (Figures 1 and S3). Further, neither the data nor the models can discriminate whether the maintenance of high viral loads is due to a lack of clearance of infected cells (i.e., long infected cell lifespan/ineffective clearance) or to the balance of new infections and clearance (i.e., short infected cell lifespan/rapid clearance coupled with rapid virus infection/production). Thus, new and more diverse data is necessary.

Viral titers remain the most frequently used data to calibrate models and assess infection dynamics. This is because collecting immunological data is more laborious and expensive. Thus, we seek models that are simple yet accurate and that can be used in the absence of immunological data. The standard viral kinetic model includes the minimal number of parameters and equations needed to recapitulate viral load dynamics. However, viral load data is insufficient to uniquely define all 6 parameters [19, 32]. Fortunately, this has not limited our ability to make robust predictions about the underlying biology or to estimate accurate parameter values even when correlations are present [12, 30, 33]. Here, the resulting parameter ensembles were well-bounded and correlations were observed in two sets of parameters (Figure 2). The correlation between the rates of virus production (p) and virus clearance (c) indicates the balance of these processes. This is expected because viral loads measure the amount of virus present and slow virus production/clearance would be indistinguishable from fast production/clearance. Similarly, the rates of infection (β) and infected cell clearance (δ_d/K_δ) were correlated, which indicates a balance of cells becoming infected and being cleared. This is visible in Figure 4B, where the log-linear fit to the data in the growth phase (red line) deviates from the model solution (black dashed line).

Analyzing infection kinetics with mathematical models provides a means to quantify different infection processes. By modeling viral load data, we can make meaningful predictions about the time scales, magnitudes, and rates of different processes even if we cannot directly define specific mechanisms. Further, having a well-characterized model allows us to design new experiments and to perform *in silico* experiments that evaluate situations where data is challenging to obtain. Here, our data, model, and analyses suggest that the clearance rate of infected cells is variable and depends on their density such that clearance slows when infected cells are numerous and fast when they are in low numbers. Understanding how the rate changes should facilitate a deeper understanding of other viral infections and of immunological data, as it becomes available. Further establishing how the virus and host components work together and how they can be manipulated will undoubtedly aid the development of therapies that prevent or treat IAV infections.

Acknowledgments

References

[1] Baccam P, Beauchemin C, Macken C, Hayden F, Perelson A (2006) Kinetics of influenza A virus infection in humans. J Virol 80(15):7590–7599

[2] Banerjee S, Guedj J, Ribeiro R, Moses M, Perelson A (2016) Estimating biologically relevant parameters under uncertainty for experimental within-host murine West Nile virus infection. Journal of The Royal Society Interface 13(117):20160,130

[3] Beauchemin C, Handel A (2011) A review of mathematical models of influenza A infections within a host or cell culture: lessons learned and challenges ahead. BMC Public Health 11(Suppl 1):S7

[4] Bender B, Small Jr P (1993) Heterotypic immune mice lose protection against influenza virus infection with senescence. J Infect Dis 168(4):873–880

[5] Best K, Guedj J, Madelain V, de Lamballerie X, Lim S, Osuna C, Whitney J, Perelson A (2017) Zika plasma viral dynamics in nonhuman primates provides insights into early infection and antiviral strategies. P Natl Acad Sci USA 114(33):8847–8852

[6] Bjornson A, Mellencamp M, Schiff G (1991) Complement is activated in the upper respiratory tract during influenza virus infection. Am Rev Respir Dis 143(5 Pt 1):1062–1066

[7] Boianelli A, Nguyen V, Ebensen T, Schulze K, Wilk E, Sharma N, Stegemann-Koniszewski S, Bruder D, Toapanta F, Guzmán C, et al (2015) Modeling influenza virus infection: a roadmap for influenza research. Viruses 7(10):5274–5304

[8] Cao P, Wang Z, Yan A, McVernon J, Xu J, Heffernan J, Kedzierska K, McCaw J (2016) On the role of CD8+ T cells in determining recovery time from influenza virus infection. Frontiers in immunology 7

[9] Douglas Jr R, Betts R, Simons R, Hogan P, Roth F (1975) Evaluation of a topical interferon inducer in experimental influenza infection in volunteers. Antimicrob Agents Ch 8(6):684–687

[10] Ghoneim H, Thomas P, McCullers J (2013) Depletion of alveolar macrophages during influenza infection facilitates bacterial superinfections. J Immunol 191(3):1250–1259

[11] Grant E, Quiñones-Parra S, Clemens E, Kedzierska K (2016) Human influenza viruses and CD8+ T cell responses. Current opinion in virology 16:132–142

[12] Gutenkunst R, Waterfall J, Casey F, Brown K, Myers C, Sethna J (2007) Universally sloppy parameter sensitivities in systems biology models. PLoS Comput Biol 3(10):e189

[13] Hayden F, Fritz R, Lobo M, Alvord W, Strober W, Straus S (1998) Local and systemic cytokine responses during experimental human influenza A virus infection. Relation to symptom formation and host defense. J Clin Investig 101(3):643

[14] Jao R, Wheelock E, Jackson G (1970) Production of interferon in volunteers infected with Asian influenza. J Infect Dis 121(4):419–426

[15] Kim T, Sun J, Braciale T (2011) T cell responses during influenza infection: getting and keeping control. Trends Immunol 32(5):225–231

[16] Larson E, Dominik J, Rowberg A, Higbee G (1976) Influenza virus population dynamics in the respiratory tract of experimentally infected mice. Infect Immunity 13(2):438–447

[17] McMichael A, Gotch F, Noble G, Beare P (1983) Cytotoxic T-cell immunity to influenza. New Engl J Med 309(1):13–17

[18] Medina R, García-Sastre A (2011) Influenza A viruses: new research developments. Nat Rev Microbiol 9(8):590–603

[19] Miao H, Xia X, Perelson A, Wu H (2011) On identifiability of nonlinear ODE models and applications in viral dynamics. SIAM Rev 53(1):3–39

[20] Neumann A, Lam N, Dahari H, Gretch D, Wiley T, Layden T, Perelson A (1998) Hepatitis C viral dynamics in vivo and the antiviral efficacy of interferon-α therapy. Science 282(5386):103–107

[21] Pawelek K, Huynh G, Quinlivan M, Cullinane A, Rong L, Perelson A (2012) Modeling within-host dynamics of influenza virus infection including immune responses. PLoS Comput Biol 8(6):e1002,588

[22] Perelson A, Neumann A, Markowitz M, Leonard J, Ho D, et al (1996) HIV-1 dynamics in vivo: Virion clearance rate, infected cell life-span, and viral generation time. Science 271(5255):1582–1586

[23] Reed L, Muench H (1938) A simple method of estimating fifty percent endpoints. Am J Epidemiol 27(3):493–497

[24] Reuman P, Bernstein D, Keefer M, Young E, Sherwood J, et al (1989) Efficacy and safety of low dosage amantadine hydrochloride as prophylaxis for influenza A. Antivir Res 11(1):27–40

[25] Simonsen L, Fukuda K, Schonberger L, Cox N (2000) The impact of influenza epidemics on hospitalizations. J Infect Dis 181(3):831–837

12

[26] Smith A (2016) Quantifying the therapeutic requirements and potential for combination therapy to prevent bacterial coinfection during influenza. J Pharmacokinet Pharm pp 1–13, DOI 10.1007/s10928-016-9494-9

[27] Smith A, McCullers J (2014) Secondary bacterial infections in influenza virus infection pathogenesis. In: Influenza Pathogenesis and Control-Volume I, Springer, pp 327–356

[28] Smith A, Perelson A (2011) Influenza A virus infection kinetics: Quantitative data and models. WIREs Sys Biol Med 3(4):429–445, DOI 10.1002/wsbm.129

[29] Smith A, Ribeiro R (2010) Modeling the viral dynamics of influenza A virus infection. Crit Rev Immunol 30(3):291–298

[30] Smith A, Smith A (2016) A critical, nonlinear threshold dictates bacterial invasion and initial kinetics during influenza. Sci Rep 6, DOI doi:10.1038/srep38703

[31] Smith A, Adler F, Perelson A (2010) An accurate two-phase approximate solution to an acute viral infection model. J Math Biol 60(5):711–726

[32] Smith A, Adler F, McAuley J, Gutenkunst R, Ribeiro R, McCullers J, Perelson A (2011) Effect of 1918 PB1-F2 expression on influenza A virus infection kinetics. PLoS Comput Biol 7(2):e1001,081

[33] Smith A, Adler F, Ribeiro R, Gutenkunst R, McAuley J, McCullers J, Perelson A (2013) Kinetics of coinfection with influenza A virus and *Streptococcus pneumoniae*. PLoS Pathog 9(3):e1003,238–e1003,238

[34] Taubenberger J, Morens D (2008) The pathology of influenza virus infections. Annu Rev Pathmechdis Mech Dis 3:499–522

[35] Thompson W, Shay D, Weintraub E, Brammer L, Bridges N CB Cox, Fukuda K (2004) Influenza-associated hospitalizations in the United States. JAMA-J Am Med Assoc 292(11):1333–1340

[36] Toapanta F, Ross T (2009) Impaired immune responses in the lungs of aged mice following influenza infection. Respir Res 10(1):112

[37] Warnking K, Klemm C, Löffler B, Niemann S, Krüchten A, Peters G, Ludwig S, Ehrhardt C (2015) Super-infection with Staphylococcus aureus inhibits influenza virus-induced type I IFN signalling through impaired STAT1-STAT2 dimerization. Cell Microbiol 17(3):303–317

Tables

Table 1: Parameters and 95% confidence intervals obtained from fitting the density-dependent model (Equations (1)–(5)) to viral titers from mice infected with 75 TCID$_{50}$ PR8.

| Parameter	Description	Units	Value	95% CI
β	Virus infectivity	TCID$_{50}^{-1}$ d^{-1}	5.5×10^{-5}	$[1.5 \times 10^{-5}, 3.8 \times 10^{-2}]$
p	Virus production	TCID$_{50}$ cell^{-1} d^{-1}	3.2	$[0.72, 100]$
c	Virus clearance	d^{-1}	18.6	$[4.1, 694]$
k	Eclipse phase	d^{-1}	4.0	$[4.0, 6.0]$
δ_d	Infected cell clearance	cell^{-1} d^{-1}	1.7×10^6	$[1.4 \times 10^6, 2.0 \times 10^6]$
K_δ	Half saturation constant	cells	1.4×10^5	$[1.5 \times 10^2, 2.5 \times 10^5]$
$T(0)$	Initial uninfected cells	cells	1×10^7	-
$I_1(0)$	Initial infected cells	cells	75	-
$I_2(0)$	Initial infected cells	cells	0	-
$V(0)$	Initial virus	TCID$_{50}$	0	-

Figures
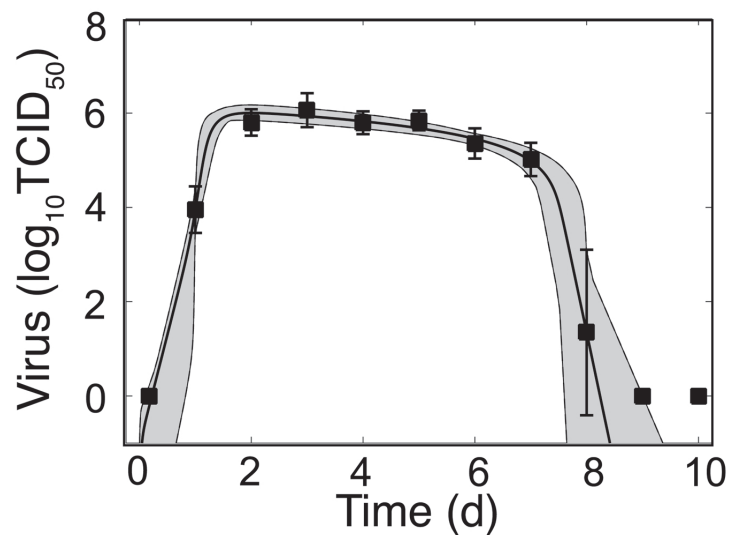
Figure 1: **Fit of the Density-Dependent Viral Kinetic Model.** Fit of the density-dependent viral kinetic model (Equations (1)–(5)) to viral lung titers from individual mice (10 mice per time point) infected with 75 TCID$_{50}$ PR8. The solid black line is the optimal solution and the gray shading is the model solution using parameter sets within the 95% CIs. Parameters are given in Table 1. Data are shown as mean $\pm$ standard deviation.
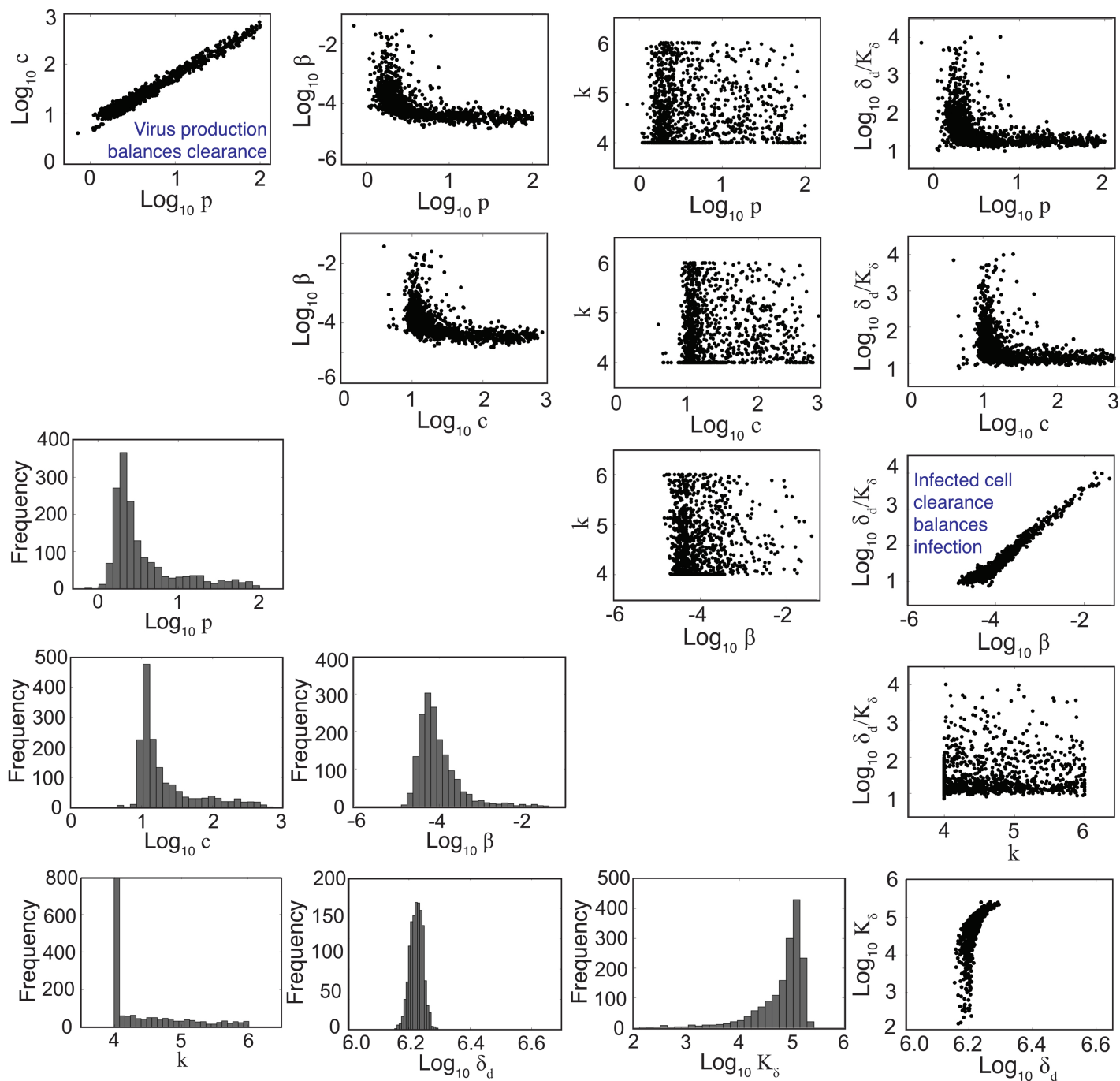
Figure 2: **Parameter Ensembles and Histograms.** Parameter ensembles and histograms resulting from fitting the density-dependent kinetic model (Equations (1)–(5)) to viral titers from mice infected with 75 TCID_{50} PR8. Two main correlations are evident between the rates of virus production (p) and clearance (c) and between the rates of infection (β) and infected cell clearance (δ_d/K_δ). The axes limits reflect imposed bounds. All parameters except the eclipse phase rate (k) are well bounded. Additional plots (e.g., for R_0) are in Figure S2.
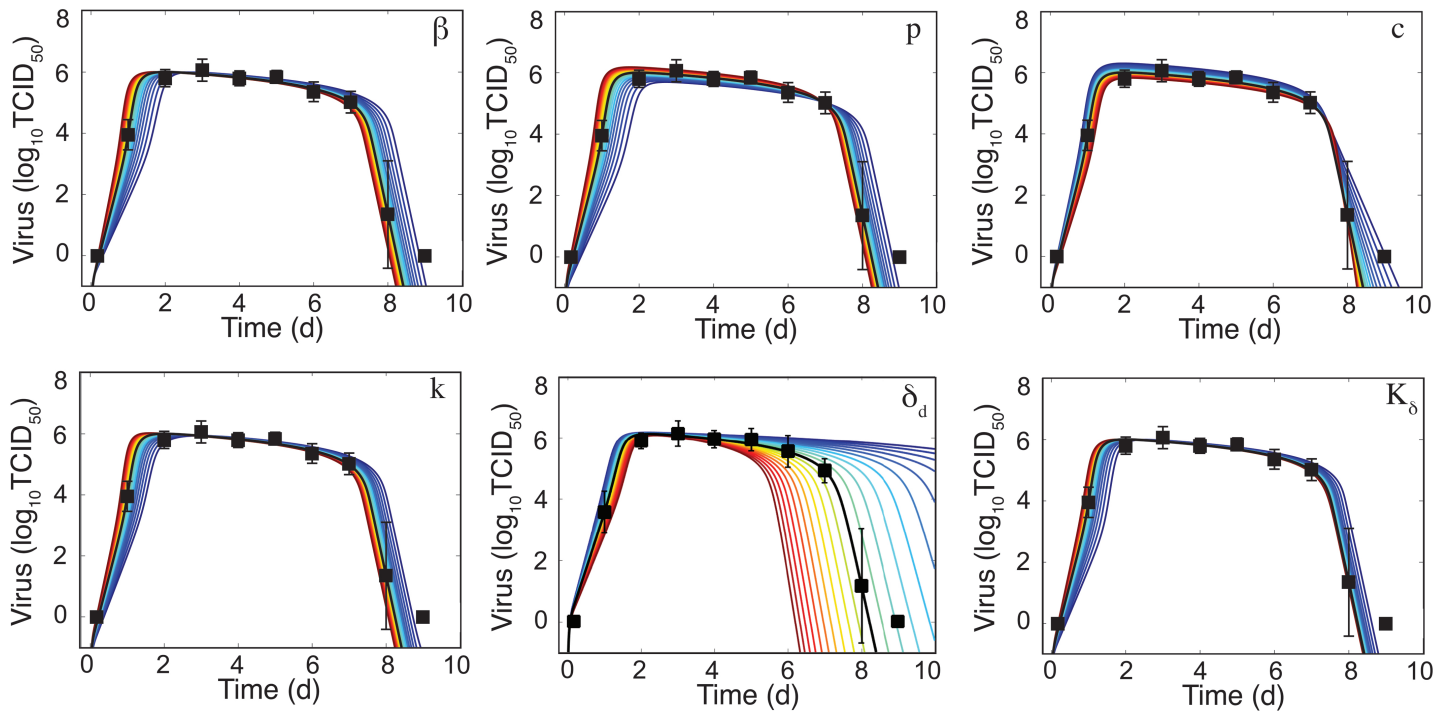
Figure 3: **Sensitivity of the Density-Dependent Viral Kinetic Model.** Solutions of the density-dependent viral kinetic model (Equations (1)–(5)) for the best-fit parameters (black line, Table 1) and with the indicated parameter increased (red) or decreased (blue) 50% from the best-fit value.
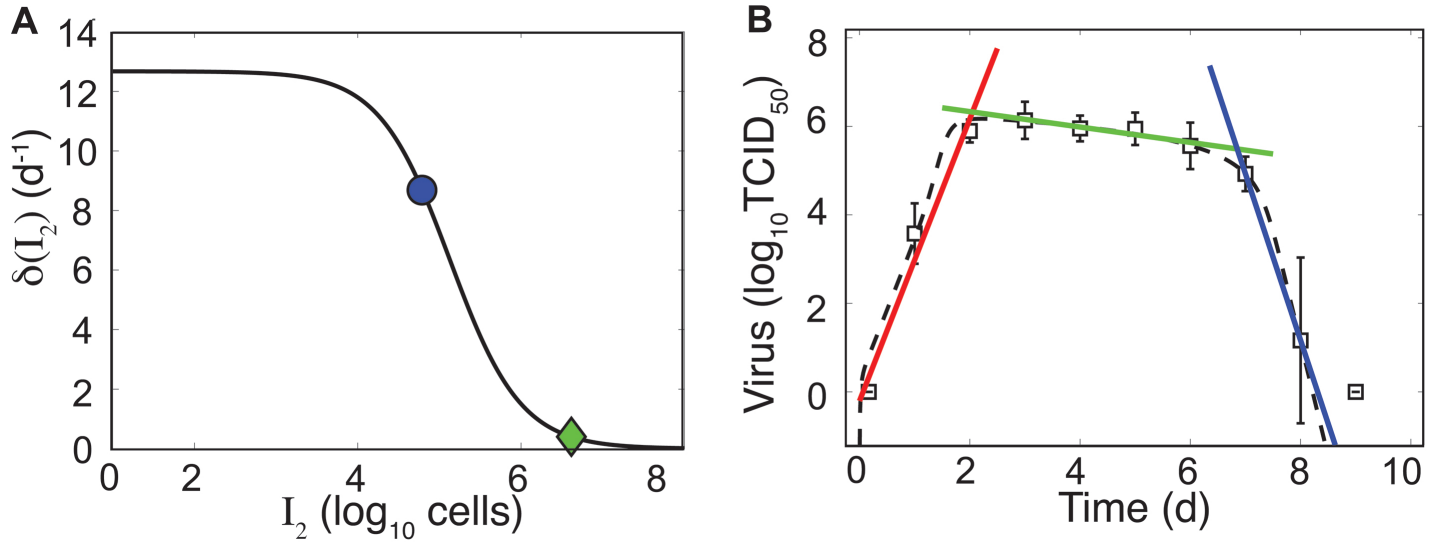
Figure 4: **Density-Dependent Infected Cell Clearance Rate and Correlation to Linear Regression.** (A) The infected cell clearance rate ($\delta(I_2)$, Equation (5)) is plotted over for different values of infected cells (I_2). The green diamond and the blue dot indicate the corresponding infected cell clearance rates during the slow and fast phases of virus clearance, respectively. These correspond to linear regression estimates in Panel B. (B) Linear regression fits to the viral load data (white squares) during the growth phase (4 h − 2 d pi, red line), the first phase of virus decay (3–6 d pi, green line), or the second phase of virus decay (7–8 d pi, blue line). The dashed black line is the fit of the density-dependent viral kinetic model (Equations (1)–(5)) to the viral load data.